nature communications

Article

https://doi.org/10.1038/s41467-024-53638-y

PilY1 regulates the dynamic architecture of the type IV pilus machine in *Pseudomonas aeruginosa*

Received: 22 December 2023

Accepted: 16 October 2024

Published online: 30 October 2024

Check for updates

Shuaiqi Guo[1,2,3] ✉, Yunjie Chang[1,2,8], Yves V. Brun[4], P. Lynne Howell[5,6], Lori L. Burrows[7] ✉ & Jun Liu[1,2] ✉

Type IV pili (T4P) produced by the pathogen *Pseudomonas aeruginosa* play a pivotal role in adhesion, surface motility, biofilm formation, and infection in humans. Despite the significance of T4P as a potential therapeutic target, key details of their dynamic assembly and underlying molecular mechanisms of pilus extension and retraction remain elusive, primarily due to challenges in isolating intact T4P machines from the bacterial cell envelope. Here, we combine cryo-electron tomography with subtomogram averaging and integrative modelling to resolve in-situ architectural details of the dynamic T4P machine in *P. aeruginosa* cells. The T4P machine forms 7-fold symmetric cage-like structures anchored in the cell envelope, providing a molecular framework for the rapid exchange of major pilin subunits during pilus extension and retraction. Our data suggest that the T4P adhesin PilY1 forms a champagne-cork-shaped structure, effectively blocking the secretin channel in the outer membrane whereas the minor-pilin complex in the periplasm appears to contact PilY1 via the central pore of the secretin gate. These findings point to a hypothetical model where the interplay between the secretin protein PilQ and the PilY1-minor-pilin priming complex is important for optimizing conformations of the T4P machine in *P. aeruginosa*, suggesting a gate-keeping mechanism that regulates pilus dynamics.

Many bacteria and archaea produce type IV pili (T4P), long, hair-like filaments that protrude from the cell surface to sense surrounding surfaces, initiate colonization, and contribute to infection[1–6]. Central to the diverse functions of T4P is their dynamic nature[3,7,8], undergoing rapid cycles of extension and retraction. This repeated assembly (extension) and disassembly (retraction) of the grappling-hook-like T4P filaments are essential for surface motility, DNA uptake, and microcolony formation by diverse bacteria[8,9].

T4P dynamics are enabled by a sophisticated, multi-protein nanomachine that spans the entire bacterial cell envelope[10]. Cryo-electron tomography (cryo-ET) studies of T4P machines in *Myxococcus xanthus*, *Thermus thermophilus*, and *Vibrio cholerae* revealed a series of

---

[1]Department of Microbial Pathogenesis, Yale School of Medicine, New Haven, CT 06536, USA. [2]Microbial Sciences Institute, Yale University, West Haven, CT 06516, USA. [3]Department of Anatomy and Cell Biology, McGill University, Montreal, QC, Canada. [4]Département de Microbiologie, Infectiologie et Immunologie, Université de Montréal, Montréal, QC, Canada. [5]Department of Biochemistry, University of Toronto, Toronto, Canada. [6]Program in Molecular Medicine, Peter Gilgan Centre for Research and Learning, The Hospital for Sick Children, Toronto, ON, Canada. [7]David Braley Center for Antibiotic Discovery, Michael G. DeGroote Institute for Infectious Disease Research, Department of Biochemistry and Biomedical Sciences, McMaster University, Hamilton, ON, Canada. [8]Present address: Department of Cell Biology and Department of Infectious Disease of Sir Run Run Shaw Hospital, Center of Cryo-Electron Microscopy, Zhejiang University School of Medicine, Hangzhou, Zhejiang, China. ✉e-mail: shuaiqi.guo@mcgill.ca; lori.burrows@mcmaster.ca; jliu@yale.edu

concentric rings anchored within the cell envelope that together constitute the basal body[5,11,12]. Within these stacked ring structures, the spatial arrangement of several T4P components has been elucidated[11]. An oligomer of PilQ forms the outer membrane secretin and connects to the alignment subcomplex, consisting of PilP, PilO, PilN, and PilM, that spans the periplasm, inner membrane, and cytoplasm. Embedded within this assembly, PilC is the inner membrane platform protein that coordinates with ATPase motors to drive assembly and disassembly of major pilin subunits into the extending and retracting pilus, respectively.

The T4P machine is crucial for the ability of the human pathogen *Pseudomonas aeruginosa* to move across surfaces, form biofilms, and initiate infection[2,4]. While individual components of *P. aeruginosa* T4P (*Pa*-T4P) have been intensively studied for the past two decades, it remains unclear how these proteins work cohesively in the nanomachine to facilitate filament extension and retraction. The multimerization state that is key to the assembly of complexes is not fully defined. The assembly of *Pa*-T4P is primed by the minor pilin proteins (FimU, PilV, PilW, PilX and PilE) and a non-pilin protein, PilY1[13–15]. Localized to the pilus tip, PilY1 acts as an adhesion protein that binds bacteria to diverse substrates[11,15–20]. In addition, PilY1 has been suggested to play key roles as a calcium-dependent regulator of twitching motility[21], a mechanosensor for surface-activated virulence of bacteria[22] and to have a regulatory role in c-di-GMP production to control surface behaviors[4,23,24]. Some other species such as *Myxococcus xanthus* produce multiple sets of minor pilins and PilY1 homologs to provide functional flexibility in various environments[18]. However, exact localization of PilY1 in various bacteria before pilus extension and how it associates with the minor pilins remain mysteries.

In this study, we use cryo-ET with subtomogram averaging and integrative modeling to elucidate the structural details of the T4P machine in *P. aeruginosa*. Our data suggest that PilY1 may form a cork-like structure that plugs the secretin gate. The interaction of PilQ and the PilY1-minor pilin subcomplex may play a key role in optimizing T4P assembly and leads us to propose a model of gate-keeping mechanism, whereby PilY1 regulates the extension and retraction of the type IV pilus.

Results

Cryo-ET and subtomogram averaging reveal that the *P. aeruginosa* T4P machine consists of four cage-like structures that span the cell envelope

Among the significant challenges in achieving high-resolution structural determination of the T4P nanomachine is the requirement to image large numbers of complexes in whole bacterial cells. Initial experiments with cryo-focused ion beam milling (cryo-FIB) and cryo-ET suggested that *P. aeruginosa* cells produce a substantially higher number of T4P nanomachines when grown as surface-attached biofilms than during liquid growth (Supplementary Fig. 1). To improve the throughput of our cryo-ET data collection workflow, we bypassed the time-consuming steps of cryo-FIB and prepared grids with surface-grown bacterial cells resuspended in a phosphate-buffered saline solution. Using a fast cryo-ET data acquisition scheme, we picked thousands of T4P nanomachine particles from just a few hundred tomograms of surface-grown *P. aeruginosa* (*Pa*) cells (Fig. 1a, Table 1). The subtomogram-averaged structures of the *Pa*-T4P machines were resolved to ~2- to 4-nm resolution (Table 1; Supplementary Figs. 2, 3), revealing many previously unknown features, including the extended c7-symmetric densities throughout the nanomachine that form four distinct cage-like structures spanning the cell envelope (Fig. 1b–e; Supplementary Fig. 4; Supplementary Movie 1).

P. aeruginosa cells that lack the retraction ATPase PilT (*ΔpilT*, T4P filaments cannot retract) produced significantly higher numbers of piliated T4P machines than wild-type cells. Thus, subtomogram averaged structures of the piliated *Pa*-T4P machine described in this study were derived from hyper-piliated *ΔpilT* cells (Fig. 1b, f). Focused refinement revealed that the upper cage of the *ΔpilT Pa*-T4P machines (~210 Å in diameter and 125 Å in height) is anchored in the double-leaflet of the outer membrane, then widens via seven elongated, spike-shaped structures that bind the peptidoglycan layer below (Fig. 1b, e–g). The mid-cage (~170 Å in diameter and 70 Å in height) sits beneath the peptidoglycan and serves as a connection point for the upper cage and inner membrane-anchoring lower cage (175 Å in diameter and 100 Å in height). The cytoplasmic cage (195 Å in diameter and 60 Å in height) appears to interact with the lower periplasmic cage within the inner membrane, and a disc-shaped structure forms its base (Fig. 1e). Furthermore, a cross-section view of piliated T4P machines showed that a pilus filament (~5.5 nm in diameter) occupies the central channel and exits the outer membrane through the upper cage (Fig. 1b, f).

TsaP helps to anchor the secretin to the peptidoglycan layer

Cryo-ET and subtomogram averaging established an architectural framework for docking high-resolution structures and structural models of *Pa*-T4P components to examine the detailed organization of the nanomachine. We first focused on resolving molecular details near the upper cage, which is primarily composed of the outer membrane-anchoring T4P secretin protein PilQ[12,25,26]. PilQ of *P. aeruginosa* has five distinct domains (Supplementary Fig. 5a). At the N terminus, two peptidoglycan-binding AMIN-like ($\mathrm{PilQ_{AMIN1\text{-}2}}$) domains are followed by the N0 and N1 domains ($\mathrm{PilQ_{N0}}$, $\mathrm{PilQ_{N1}}$) with a secretin domain ($\mathrm{PilQ_{Secretin}}$) at the C-terminus. Single-particle cryo-EM revealed that the *P. aeruginosa* $\mathrm{PilQ_{Secretin}}$ interweaves into a C_{14} symmetric β-barrel, while the 14 $\mathrm{PilQ_{N1}}$ form a ring-shaped structure below[25,27]. The N-terminal $\mathrm{PilQ_{AMIN1\text{-}2}}$ and $\mathrm{PilQ_{N0}}$ domains were not visible in the purified in vitro full length cryo-EM structure[27]. The cryo-EM structure of $\mathrm{PilQ_{N1\text{-}secretin}}$ (PDB: 6ve3) was docked into the central interior of the upper cage anchored to the outer membrane (Fig. 1g). Intriguingly, an additional cryo-ET density not observed in the cryo-EM structure of $\mathrm{PilQ_{N1\text{-}secretin}}$ surrounds the secretin periphery (Fig. 1g) and extends further downward to form c7-symmetric spike-shaped structures in contact with the peptidoglycan layer (Fig. 1g, h). Single-particle cryo-EM demonstrated that TsaP, a T4P protein implicated in surface sensing, forms a belt-shaped structure around $\mathrm{PilQ_{N1\text{-}secretin}}$ via its C-terminal two tandem β-roll domains (herein referred to as $\mathrm{TsaP_{CI\text{-}II}}$), with an overall stoichiometry of seven TsaP to fourteen PilQ[27] (Supplementary Fig. 5b, c). The structure of the $\mathrm{PilQ_{N1\text{-}secretin}}$-$\mathrm{TsaP_{CI\text{-}II}}$ complex (PDB: 6ve2) fits well into the cryo-ET density ($\mathrm{CC_{mainchain}} = 0.65$, Supplementary Table 1), confirming that the c7-symmetric belt around PilQ is likely formed by the $\mathrm{TsaP_{CI\text{-}II}}$ domains in situ (Fig. 1g, h). Interestingly, despite limited shared sequence identity, the architecture of the *Pa*-T4P secretin-TsaP complex resembles that of the secretin-pilotin complex from the *Pa* Tight Adherence Secretion System recently resolved by cryo-EM single-particle analysis[28]. It was also proposed that TsaP might replace the pilotin PilF after the proper insertion of PilQ in the outer membrane[27].

Both PilQ and TsaP have peptidoglycan (PG)-binding modules in their N termini ($\mathrm{PilQ_{AMIN1\text{-}2}}$ and $\mathrm{TsaP_{LysM}}$)[29], but neither was observed in the cryo-EM structures, as PG is absent in purified secretin preparations. The cryo-ET density of seven extended spikes extends from $\mathrm{TsaP_{CI\text{-}CII}}$ to contact the PG (Fig. 1g, h). To investigate if these structures are the PG-binding $\mathrm{TsaP_{LysM}}$, we imaged a *tsaP*-deletion (*ΔtsaP*) strain and solved the subtomogram-averaged structure of its T4P machine. Deletion of *tsaP* caused both the belt-shaped structure around PilQ and the PG-connecting spikes to disappear (Fig. 2a, b in comparison to Fig. 1f, g). This finding indicates that TsaP is indeed a main component of the c7-symmetric spike and likely helps to anchor the secretin to the peptidoglycan layer. Most T4P machines in the *ΔtsaP* mutant cells (>90%) are in the non-piliated state (Supplementary Fig. 5d, e). The central channel of the *ΔtsaP* T4P machine contains a rod-like structure thinner (~4.2 nm, Fig. 2a) than the type IV pilus filament (~5.5 nm, Fig. 1f). Based on cryo-ET studies of the T4P machine in *M. xanthus*[11,18], this rod-like structure is likely the minor pilin complex (Fig. 2b). Moreover, an unknown structure near the outer membrane plugs the secretin of the non-piliated *ΔtsaP* T4P machine from above and appears to be in contact with the minor pilin complex below (Fig. 2a, b). This cork-like structure is also observed in the non-piliated structure of the *ΔpilB Pa*-T4P machine (Fig. 1c).

Pseudoatomic assembly of the outer membrane-associated secretin and associated proteins

To further dissect the molecular details of the secretin and its associated proteins, we used AlphaFold-Multimer (ColabFold v1.5.3 with alphafold2_multimer_v3) to predict the structure of the monomeric PilQ-TsaP complex[30,31] and then modeled the assembly with a stoichiometry of 14:7, as demonstrated by cryo-EM (Fig. 2c; Supplementary Fig. 5c, left, Supplementary Fig. 6b). The core architecture of the PilQ-TsaP model follows that of the cryo-EM structure of the PilQ$_{\text{N1-secretin}}$-TsaP$_{\text{CI-II}}$ complex. In

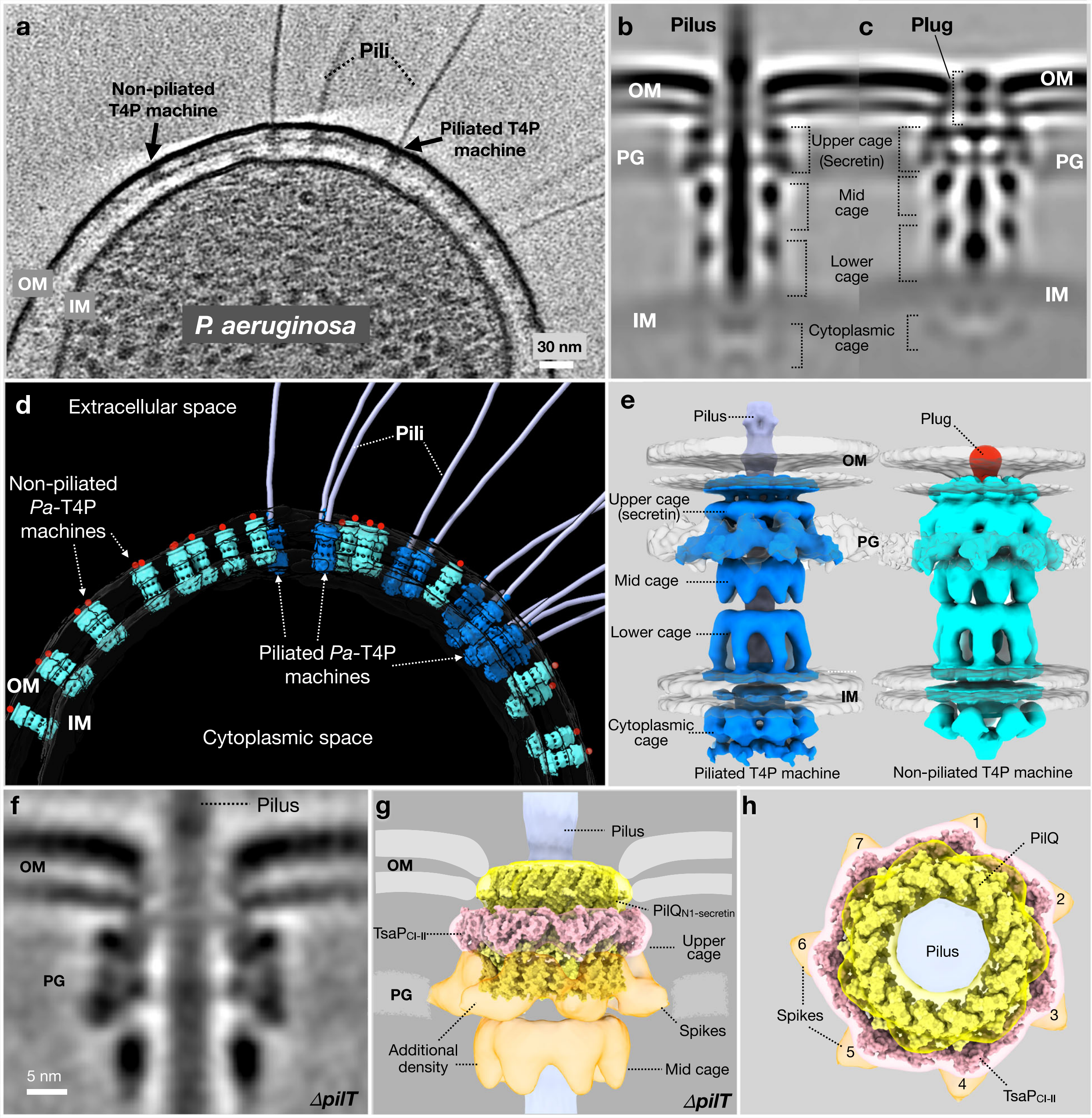

Fig. 1 | The in-situ architecture of the *P. aeruginosa* T4P machine reveals a cage-like structure that spans the cell envelope. **a** Slice through a tomogram of the cell pole of a wild-type *P. aeruginosa* (similar results were observed in >100 tomograms). **b** Central slice of the subtomogram-averaged structure of the piliated T4P machine from the *ΔpilT* cells of *P. aeruginosa*. **c** Central slice of the subtomogram-averaged structure of the non-piliated T4P machine from the *ΔpilB* cells of *P. aeruginosa*. **d** Subtomogram-averaged structures of the piliated (14) and non-piliated (64) *Pa*-T4P machines are mapped back into the segmented bacterial membranes of the tomogram shown in (**a**). Also see Supplementary Movie 1. **e** In-situ architectures of the piliated *ΔpilT* and non-piliated *ΔpilB Pa*-T4P machines assembled from segmented focus-refined maps (**f**, Fig. 4g; Supplementary Fig. 8a, b) of the nanomachine. OM outer membrane, PG peptidoglycan, IM inner membrane. **f** Central slice of the focus-refined subtomogram-averaged structure of the upper and mid-cage regions of the piliated *ΔpilT* T4P machine. **g** Cryo-EM single-particle structure of *P. aeruginosa* secretin PilQ$_{\text{N1-secretin}}$ (PDB: 6ve2/EMDB ID: EMD-21152, secretin gate opened to accommodate the pilus) in complex with TsaP$_{\text{CI-II}}$ (pink) fitted into the subtomogram-averaged map of the upper and mid-cage of the T4P machine[27]. **h** Top view of the upper cage.

Table 1 | Strains, cryo-ET data, and estimated resolution of structures in this manuscript

Strain	Pixel size (Å)	Tomogram No.	Subtomogram No.	Estimated Resolution FSC$_{0.5}$ (Å)	EMDB IDs
ΔpilB (Global)	2.148	283	5214	38.6	EMD-43434
ΔpilB (Upper + mid cages)	2.148	283	1173	24.1	EMD-43410
ΔpilB (Mid + lower cages)	2.148	283	1627	28.7	\
ΔpilT (Global)	2.148	228	4054	41.1	EMD-43418
ΔpilT (Upper + mid cages)	2.148	228	1128	27.7	EMD-43426
ΔpilT (Mid + lower cages)	2.148	228	507	32.0	
ΔtsaP (Global)	2.148	162	2213	47.9	\
ΔtsaP (Upper + mid cages)	2.148	162	1514	31.3	EMD-43433
ΔpilY1 (Global)	2.148	250	3819	38.5	\
ΔpilY1 (Upper + mid cages)	2.148	250	2182	29.4	EMD-43432

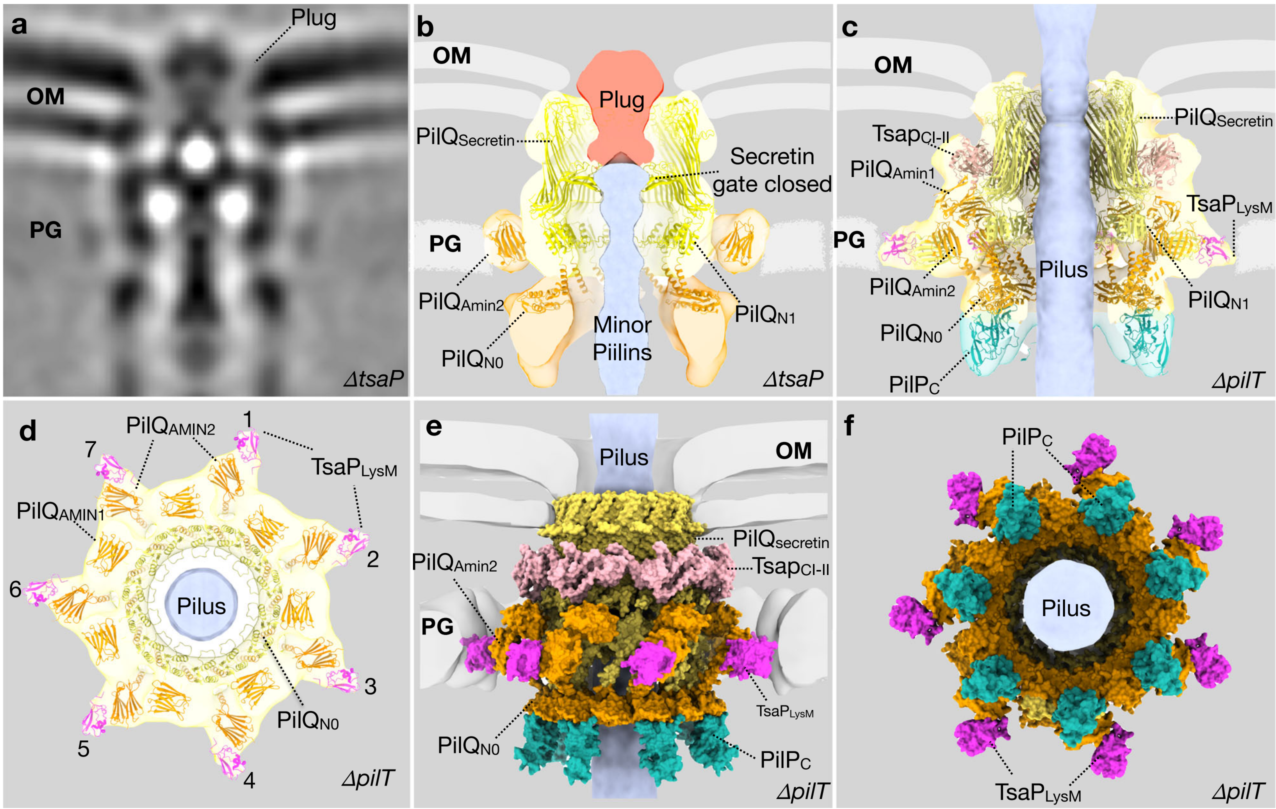

Fig. 2 | Structural details of the secretin and its interface with the alignment subcomplex. a Central slice of the focus-refined subtomogram-averaged structure of the upper and mid-cage regions of the T4P machine from *ΔtsaP* cells. **b** Structure of PilQ (yellow for PilQ$_{N1\text{-}secretin}$ solved by cryo-EM (PDB:6VE3/EMDB ID:EMD-21153) and orange for PilQ$_{Amin2}$ and PilQ$_{N0}$ structures predicted by AlphaFold) fitted into the subtomogram-averaged map of the *Pa*-T4P machine from *ΔtsaP* cells. **c** Structure of PilQ (yellow for PilQ$_{N1\text{-}secretin}$ solved by cryo-EM and orange for the PilQ$_{Amin1,2\text{-}N0}$ structure predicted by AlphaFold) in complex with TsaP (pink for TsaP$_{CI\text{-}II}$ solved by cryo-EM and magenta for TsaP$_{LysM}$ predicted by AlphaFold) and PilP$_{C}$ fitted into the segmented subtomogram-averaged map of piliated *Pa*-T4P machines from *ΔpilT* cells. **d** Cross-section view of the *Pa*-T4P machine derived from the hyperpiliated *ΔpilT* cells showing its extended shape that contacts PG. **e** Pseudoatomic structure of the PilQ-TsaP-PilP$_{C}$ complex anchored within the segmented cryo-ET density of OM and PG in the piliated *ΔpilT Pa*-T4P machine. **f** Surface representation view of the bottom of the PilQ-TsaP-PilP$_{C}$ complex in the piliated *ΔpilT Pa*-T4P machine.

addition, the PilQ-TsaP model shows that the seven copies of the TsaP$_{LysM}$ and the PilQ$_{AMIN1\text{-}2}$ domains protrude from the secretin, forming extended, spike-shaped structures (Supplementary Fig. 5c, right). Below PilQ$_{Secretin}$, the PilQ$_{N1}$ domains form a ring-shaped structure under the secretin gate in the periplasmic space (Fig. 2c). The PilQ$_{N0}$ ring is situated beneath the PilQ$_{N1}$ ring, which serves as a hub linking the secretin to the extended, peptidoglycan-binding PilQ$_{AMIN1\text{-}2}$ domains on the periphery (Fig. 2c). The core of PilQ-TsaP fits into the upper cage density near the outer membrane (Fig. 2c, d), where the c7-symmetric spikes in contact with PG most likely consist of the TsaP$_{LysM}$ and PilQ$_{AMIN1\text{-}2}$ domains (Fig. 2c, d). Although 14 copies of PilQ$_{AMIN1\text{-}2}$ were expected, only 7 copies could be fitted into the subtomogram-averaged density. We speculate that these 7 PilQ$_{AMIN1\text{-}2}$ might be stabilized by the corresponding 7 TsaP$_{LysM}$ at 1:1 ratio, whereas the other 7 copies of PilQ$_{AMIN1\text{-}2}$ are too dynamic to be visible in the subtomogram-averaged density. Consistent with the hypothesis that TsaP$_{LysM}$ is a component of the c7-symmetric spikes, the core of PilQ$_{N0\text{-}secretin}$ fits well into the subtomogram-averaged map of the *ΔtsaP* T4P machine (CC$_{mainchain}$ = 0.73, Supplementary Table 1) while the belt-like structure around the PilQ$_{Secretin}$ and most of the peptidoglycan-interacting spikes are absent (Fig. 2b).

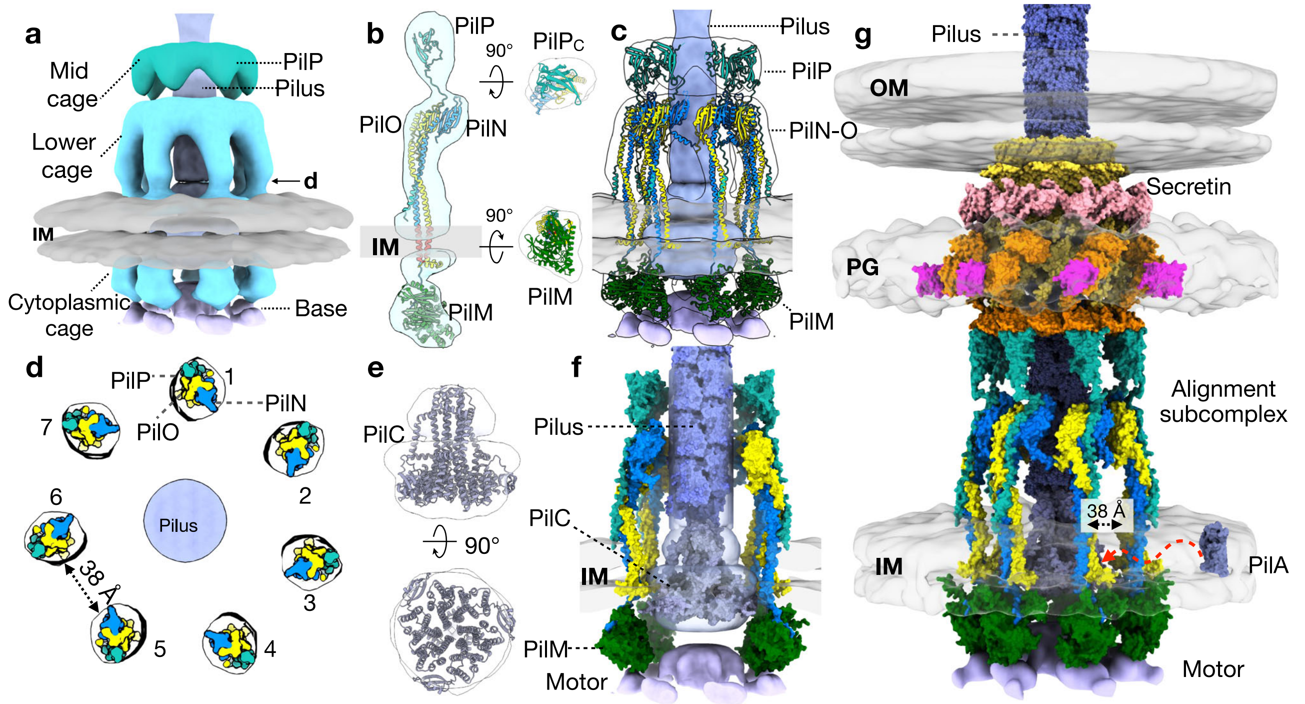

Fig. 3 | In-situ architecture of the *P. aeruginosa* T4P machine. **a** Segmented focus-refined map (raw density map in Supplementary Fig. 8a) of the lower and cytoplasmic cage regions of the piliated T4P machine. **b** AlphaFold-Multimer-predicted structure of the PilP (light green)–PilO (yellow; transmembrane region, red)–PilN (blue; transmembrane region, red)–PilM (dark green) complex fitted into the segmented cryo-ET map (transparent). **c** Architecture of the c7-symmetric alignment subcomplex fitted into the subtomogram-averaged cryo-ET map. The cryo-ET maps are transparent, with the structures docked in their interiors. **d** Cross-section view of the lower periplasmic cage that shows the c7-symmetry complex PilP-PilO-PilN surrounding the pilus in the center. The relative position of (**d**) is shown with an arrow in (**a**). The spacing between two neighboring pillars (composed of PilP-N-O) is ~38 Å, which enables the free diffusion of major pilin PilA to enter and exit the T4P machine within the inner membrane. **e** PilC trimer model fitted into the segmented cryo-ET density. **f** Cross-section view of the T4P machine showing the AlphaFold-predicted PilC trimer and the cryo-EM structure of the *P. aeruginosa* PAO1 T4P filament (PDB: 8TUM) fitted into the segmented cryo-ET maps. The motor (light blue) is illustrated with the cryo-ET density. **g** In-situ architectural model of the piliated T4P machine of *P. aeruginosa*.

The remaining structures that contact the peptidoglycan were fitted with PilQ$_{AMIN1/2}$ given their proximity to the PilQ$_{NO}$ domains (Fig. 2b). The 14 PilQ$_{NO}$ domains extend into the mid-cage below the upper cage (Fig. 2b). The presence of the additional c7-symmetric density further beneath PilQ$_{NO}$ suggests that the mid-cage is composed of other T4P machine components intimately associated with the secretin (Fig. 2b). Given that the secretin PilQ interacts with the alignment subcomplex protein PilP[32], we predicted their interactions using AlphaFold-Multimer (Fig. S6a, c). Consistent with the biochemical data[33], the predicted PilQ-PilP complex suggests that PilQ interacts with the C-terminal β-sandwich domain of PilP (PilP$_C$) via its N0 domain. Whereas the N-terminal domain of PilP (PilP$_N$) appears to be largely unstructured, with only a short α-helical region (Supplementary Figs. 6a, c, 7a). The PilQ$_{NO}$ -PilP$_C$ complex is in excellent agreement with the density of the mid-cage (Fig. 2c; CC$_{mainchain}$ = 0.85; Supplementary Table 1, Supplementary Fig. 7b, c), revealing the dynamic interface between the secretin and alignment subcomplex in the periplasmic space (Fig. 2c, e, f). Interestingly, the PilQ$_{NO}$ -PilP$_C$ interface resembles that of the GspCHR:GspDN0-N1 complex in the Type II secretion system of *E. coli*[34]. Overall, the integrative structural biology approach described above enabled us to model the assembly of the secretin and its binding partners into the in-situ cryo-ET map in a stoichiometry-specific manner, providing a solid foundation for building an accurate model of the intact T4P machine in *P. aeruginosa*.

In-situ architecture of the intact *Pa* T4P machine

Having resolved the PilQ$_{NO}$-PilP$_C$-mediated secretin-alignment subcomplex interface, we next examined the structural details that are key for the stoichiometry-dependent assembly of the large inner membrane-associated periplasmic and cytoplasmic c7-symmetric cage-like structures (Fig. 3a; Supplementary Fig. 8a), which correspond to four T4P proteins: PilM, PilN, PilO, and PilP[11,35].

X-ray crystallography and biochemical studies indicated that PilN and PilO form a heterodimer using their ferredoxin-like globular C-terminal domains rich in β sheets[35–38]. This dimerization interface is preserved in the complex predicted by AlphaFold-Multimer (Fig. 3b; Supplementary Figs. 6e, 8c). Interestingly, AlphaFold-Multimer further suggested that the N-terminal domains of PilN and PilO intertwine to form an extended, coiled-coil-like structure (Fig. 3b; Supplementary Fig. 8c, f, g). The α-helical regions of both PilN and PilO have transmembrane segments near their N termini, thereby anchoring the heterodimeric complex in the inner membrane (Fig. 3b; Supplementary Fig. 8c). While PilP$_C$ adopts a β-sandwich fold, AlphaFold-Multimer predicted that PilP$_N$ has an extended shape that interacts with the PilN-PilO coiled-coil via its short α-helix, together forming a tri-helix-bundle-like structure (Fig. 3b; Supplementary Figs. 6g, 8c). The predicted PilP$_N$ is shorter than the PilN-PilO helices (Fig.3b; Supplementary Fig. 8c), consistent with PilP$_N$ lacking a transmembrane helix. Instead, PilP is lipidated at cysteine 18 after removal of its N-terminal 17-aa signal sequence[32,33], and the lipid moiety anchors PilP in the outer leaflet of the inner membrane (Supplementary Fig. 8c, right).

Further, the 9 N-terminal residues of PilN protrude into the cytoplasm, where they form a complex with the cytoplasmic protein PilM[39–41] (Supplementary Fig. 8c, d), thereby linking the periplasmic and cytoplasmic components of the T4P machine. Combining these extensive biochemical and structural findings, a trans-inner membrane tetrameric complex of PilP-PilN-PilO-PilM was assembled (Fig. 3b). The PilP-PilN-PilO-PilM complex predicted by AlphaFold-Multimer has an extended pillar shape that fits well into the segmented cryo-ET density map (Fig. 3b; $CC_{mainchain} = 0.65$, Supplementary Table 1). Interestingly, a PilN-O-M complex was also recently identified in the flagellar motor of *Helicobacter pylori* and plays a key role in regulating its motility[42]. Given that seven copies of the tetrameric complex form the alignment subcomplex cage, the spacing between each pillar in the inner membrane and periplasm is ~38 Å (Fig. 3d, g). This size of this opening is sufficient to allow monomers of major pilin PilA, which has dimensions of 48 × 24 × 34 Å, to freely diffuse through the PilP-PilN-PilO cage to interact with the platform protein, allowing pilin assembly into a growing pilus or extraction from a retracting filament (Fig. 3c, d, f, g)[43,44]. The Type IV pilus has a diameter of ~5.5 nm in the subtomgram averaged structure (Fig. 3f; Supplementary Fig. 8a), which is in excellent agreement with recently resolved structures of the *P. aeruginosa* PAO1 T4P filament (PDB: 8TUM; also see Ochner et al.[45], BioRxiv)[46].

The pear-shaped, inner membrane-embedded density at the base of the pilus filament is likely the platform protein PilC, as identified in *M. xanthus* by cryo-ET[11] (Fig. 3e, f; Supplementary Fig. 8a, b). Recent modeling and experimental data suggested that PilC and its homologs in the T2SS form a trimer that interacts with hexameric ATPases in the cytoplasm[47,48]. We generated the PilC-trimer structure using AlphaFold-Multimer, which was then docked into the pear-shaped inner membrane-embedding density (Fig. 3e, f; $CC_{mainchain} = 0.6$, Supplementary Table 1). In addition, a disc-shaped density is nestled between the seven PilM molecules below PilC in the cytoplasm, forming the base of the cytoplasmic cage (Fig. 3a, c, f; Supplementary Fig. 8a). This structure likely represents one of the ATPase motors (PilB, PilU, or PilT) of the *Pa* T4P machine. As this structure is observed in the piliated structure when the retraction ATPase PilT is deleted (*ΔpilT*), we speculate it may be the extension ATPase PilB. Although the resolution was insufficient to resolve details of direct contact between PilC and the ATPase motor, this integrative approach enabled us to build a near-complete pseudoatomic structure of the type IV pilus machinery of *P. aeruginosa* (Fig. 3g; Supplementary Movie 1).

PilY1 may form a cork-like structure that plugs the T4P machine in the outer membrane

Having revealed the structural details of the piliated nanomachine at ~30 Å resolution (Table 1), we next examined the architecture of the *Pa*-T4P machine in the non-piliated state to further gain insights into the molecular mechanisms of pilus extension and retraction. We resolved the *Pa*-T4P machines from cells lacking the extension ATPase PilB (*ΔpilB*), where T4P machines are locked in their non-piliated state. Cross-section view of the subtomogram-averaged *ΔpilB Pa*-T4P machine at ~38.6 Å resolution revealed a thin, rod-like minor pilin subcomplex that threads through the central cavities of the lower and mid cages (Fig. 1c). Focused refinement near the upper and mid cages of the *ΔpilB Pa*-T4P machine at 26 Å resolution revealed that the top part of the minor pilin subcomplex presses against the secretin gate in its closed state (Fig. 4g; Table 1). Intriguingly, a two-lobed, champagne-cork-shaped density of unknown identity plugs the outer membrane cavity and is in direct contact with the secretin gate and the apex of the minor pilin complex (Figs. 4g, 2a). We reasoned that, as the major pilin subunit PilA begins to be incorporated into the pilus near the inner membrane, the pilus grows in length, and will push upward to force open the secretin gate. As the plug capping the minor pilin complex is localized to the pilus tip, we speculated that the cork-shaped density is the tip adhesin PilY1 which binds to diverse surfaces in a T4P-dependent manner[4,15,21,22,49,50].

To test this key hypothesis, we determined the subtomogram-averaged structure of the T4P machine from *pilY1* deletion mutant (*ΔpilY1*) cells (Fig. 4a–f). Consistent with reports that PilY1 is required to prime extension of the pilus, all T4P machines observed in the *ΔpilY1* cells are in a non-piliated state (Fig. 4a). Strikingly, subtomogram averaging revealed that the cork-shaped density plugging the non-piliated machine disappeared from the *ΔpilY1* T4P machines, leaving a large oval-shaped cavity in the outer membrane above the upper cage (Fig. 4b–f). The edge of this cavity bends inwards ~15° compared to the plugged T4P machine (Fig. 4f, g; Supplementary Fig. 10b, d, f, h), suggesting that the structure directly interacts with and modulates the conformations of PilQ and its interaction with the outer membrane. Moreover, subtomogram-averaged densities for the alignment subcomplex as well as the minor pilin subcomplex below the secretin gate are significantly diminished (Fig. 4b–f; Supplementary Fig. 10b, d). 3-D classification further demonstrated the highly dynamic nature of the *Pa*-T4P machine in the absence of PilY1 where local spacing of the periplasmic space appeared to be modulated by assembly of the alignment subcomplex (Fig. 4b–e). Since the T4P components are interconnected throughout the cell envelope, this result suggested that the removal of PilY1, which led to disappearance of the plug-shaped density, has a significant impact on the overall dynamics and architecture of the T4P machine. Taken together, these genetic and in-situ structural data support our hypothesis that the cork-shaped density is PilY1, and its interaction with the secretin and minor pilin complex is important for optimizing T4P conformations.

PilY1 likely interacts with the secretin near the outer membrane

In the *Pa* PAO1 strains used here, PilY1 is a ~126-kDa protein with two distinct regions: a 51-kDa N-terminal region containing a von Willebrand factor type A (vWA)-like domain that serves as an adhesin module in diverse proteins[50–53] and a C-terminal seven-bladed β-propeller fold, as revealed by X-ray crystallography[21]. AlphaFold2 predicted that full-length PilY1 has a compact two-lobed architecture that fits neatly into the champagne-cork-shaped cryo-ET density (Fig. 4h, i; $CC_{mainchain} = 0.67$, Supplementary Table 1; Supplementary Fig. 11). The vWA-like domain has a Rossmann fold with a central 5-strand parallel β-sheet flanked by 6 α-helices (Fig. 4h, magenta; Supplementary Fig. 11). The conserved metal-ion-dependent adhesion site (MIDAS) of the PilY1 vWA domain points upward (Fig. 4h, Fig. S11), which is exposed to the extracellular environments. Notably, a small intervening domain is inserted between the first β and α elements of the Rossmann fold and situated laterally to the vWA domain, above the β-propeller (Fig. 4h, orange; Supplementary Fig. 11). The β-propeller has an overall c7-symmetric funnel-like shape with a small hollow interior (Fig. 4h, right; Supplementary Fig. 11). While its narrower end directly interacts with the vWA domain and the insert domain above, the wider end of the funnel-shaped structure composed of the seven β-blades is in contact with the dynamic secretin gate and the apex of the minor-pilin subcomplex (Fig. 4i, j). Although the resolution of the cryo-ET map is insufficient to resolve detailed protein-protein interactions, predicted association of seven blades with the c14-symmetric secretin gate of PilQ hints at a stoichiometry-dependent interaction between the two proteins.

Discussion

Over the past two decades, structures of nearly all *Pa*-T4P core components have been resolved to high resolution by X-ray crystallography and cryo-EM single-particle analyses. The recent development of AlphaFold-Multimer has substantially improved the accuracy of macromolecular complex modeling. Taken together with the subtomogram-averaged structures of the *Pa*-T4P machine solved at higher resolution, our integrative in-situ structural biology approach enabled us to discover crucial details that govern the assembly of this dynamic nanomachine. The challenges of producing a high number of the nanomachines in native bacterial cells for visualization by cryo-ET were a major hurdle that hampered high-resolution structural determination of the T4P machines. Serendipitously, our cryo-FIB and cryo-ET analyses of *P. aeruginosa* colony biofilms revealed that surface attachment markedly enhanced T4P production, thereby increasing

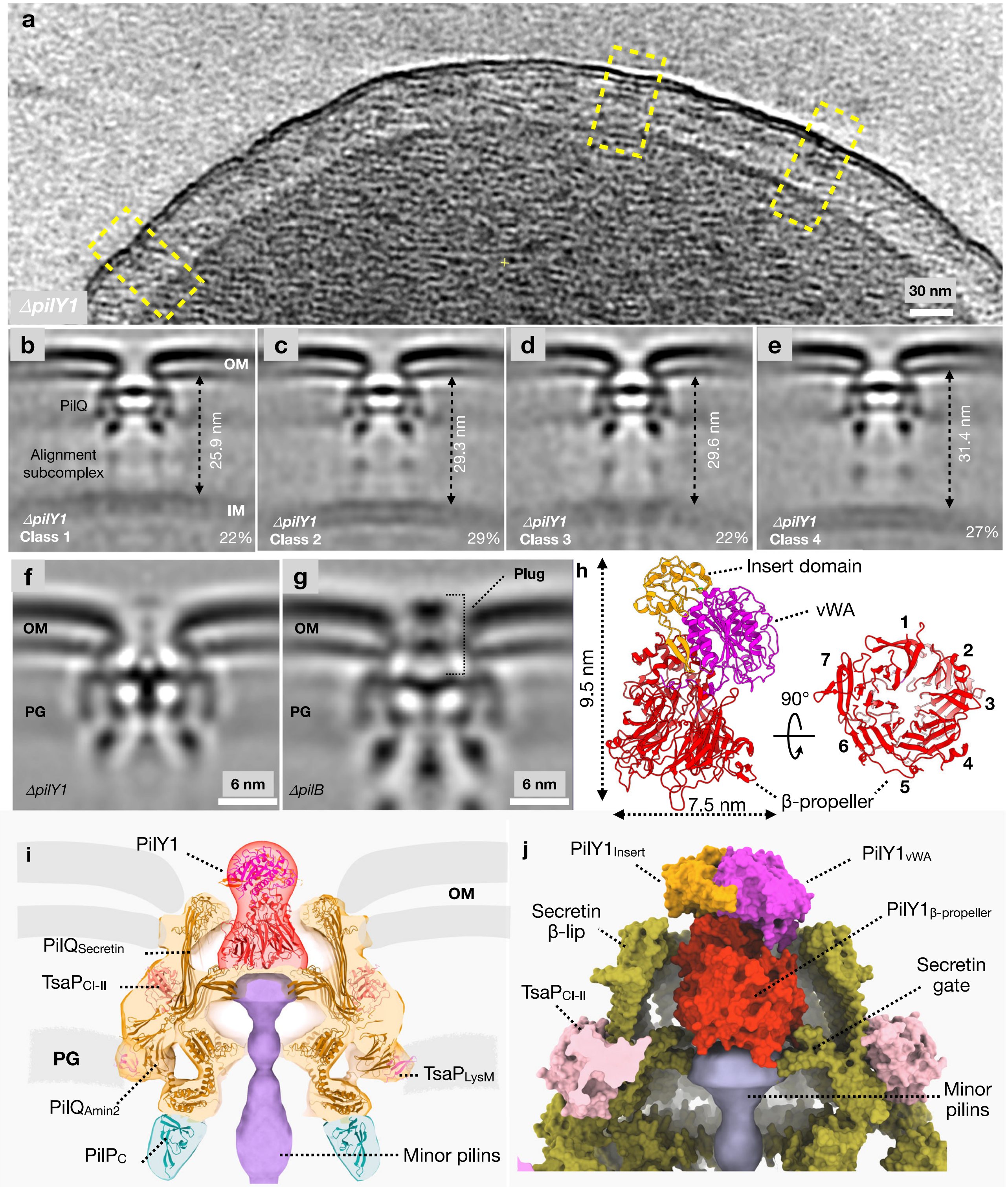

Fig. 4 | Proposed role of PilY1 in regulating the dynamic T4P architectures. a A central slice of a tomogram of *ΔpilY1* cells (similar results were observed in >100 tomograms). Yellow boxes indicate some of the T4P machines seen in the tomogram. **b**–**e** 3-D classification of the subtomogram-averaged structure of the *ΔpilY1 Pa*-T4P machine. The percentage of the particles and spacing of the periplasm are indicated. **f** Central slice of the focus-refined subtomogram-averaged structure of the top region of the *ΔpilY1* T4P machine. **g** Central slice of the focus-refined subtomogram-averaged structure of the top region of the non-piliated *ΔpilB* T4P machine. **h** Structure of PilY1 predicted by AlphaFold2. **i** AlphaFold predicted structure of PilQ in complex with TsaP, $PilP_C$, and PilY1 fitted into the focus-refined subtomogram-averaged maps of the *ΔpilB* T4P machine. **j** A zoomed-in view of (**i**) where PilY1 interacts with PilQ and the minor pilin complex. Insert domain, orange; vWA domain, magenta; β-propeller domain, red.

the number of observed *Pa*-T4P machines per cell by over 10-fold (Table 1; Supplementary Fig. 1). This is consistent with the literature showing that T4P play key roles in intercellular and bacterium-surface interactions during the early stage of biofilm formation[2,3,50,54] (Fig. 5a).

To further increase throughput of cryo-ET data collection, we chose to bypass the time-consuming cryo-FIB procedures and imaged hundreds of cell tips of individual bacteria from colony biofilms grown on solid agar surface. Using a fast tilt series data collection scheme[55], we

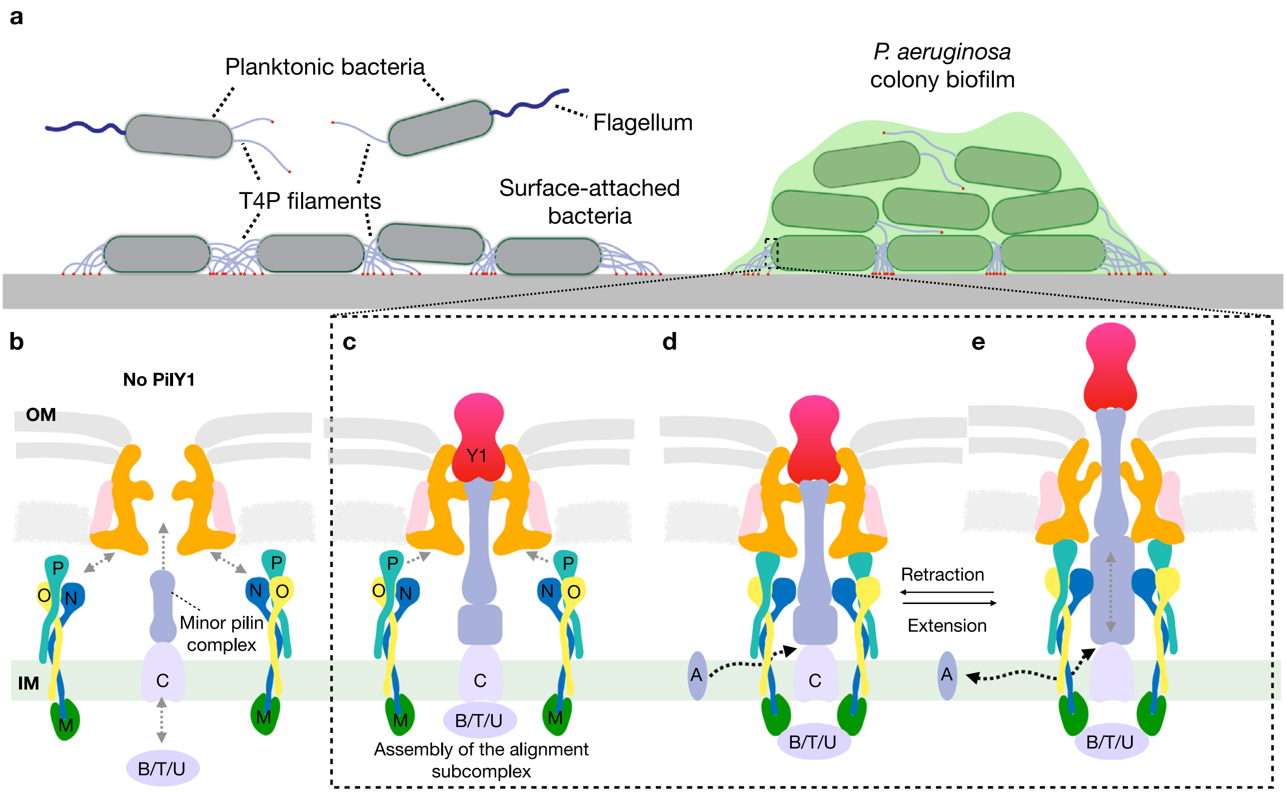

Fig. 5 | Proposed model of the dynamic assembly of the *Pa*-T4P machine. **a** Compared to those in the planktonic state, surface-attached *P. aeruginosa* overproduce T4P leading to formation of biofilms. Parts of (**a**) were created in BioRender. Guo, S. (2024) BioRender.com/n16p426. **b** In the absence of PilY1, the assembly of the minor pilin and the alignment subcomplexes is suboptimal. **c** PilY1 and the minor pilin complex help optimize the conformations of the T4P machine for pilus dynamics. **d**, **e** PilY1 assembles to the pilus tip via the minor-pilin complex during the dynamic cycles of T4P extension and retraction.

acquired higher numbers of subtomograms of the *Pa*-T4P machines in various mutant strains. These rich datasets enabled the elucidation of the dynamic architectures of the *Pa*-T4P machine through extensive 3-D classification, revealing previously unknown features of the nanomachine at various stages of pilus extension and retraction (Supplementary Movie 1).

The basal body of the *Pa*-T4P machine has a 14:7 stoichiometry spanning the cell envelope, with the outer membrane-peptidoglycan-anchored secretin PilQ connected with the inner membrane-protruding alignment subcomplex comprised of the PilP-O-N-M proteins. TsaP surrounds the secretin and further anchors the T4P machine to the peptidoglycan. Thus, in addition to TsaP's proposed role in helping *P. aeruginosa* sense surfaces[27], it also likely contributes to brace the nanomachine against extraordinary forces generated during pilus retraction. Notably, we propose that the secretin pore is obstructed by the pilus tip protein PilY1 in the non-piliated state. PilY1 has a two-lobed structure that appears to interact with the outer membrane-associated β-lips and central gate of the secretin as well as the apex of the minor pilin complex. T4P machines in *ΔpilY1* cells have no pili and significantly diminished density for structures below PilQ, indicating they have become more dynamic (Fig. 4b–f; Supplementary Fig. 10). Thus, PilY1 and the minor pilin complex may potentially modulate the structure of PilQ, and their interaction is likely important in orchestrating the orderly assembly and the stability of the alignment subcomplex below. Our data suggest that in non-piliated T4P machines, the minor pilin subcomplex forms a rod-like structure within the alignment subcomplex that may interact with PilY1 on the outside of the secretin gate exposed to the extracellular space (Figs.1c, 4g). Bioinformatic analyses and biochemical data have shown that the minor pilin proteins PilVWX and the non-pilin PilY1 form a priming complex for T4P extension[15,18]. Given its large dimension with a height of ~95 Å and diameter of over 70 Å, PilY1 in its folded state cannot diffuse through the alignment subcomplex cage (~38-Å-wide spacing, Fig. 3d, g). Therefore, the dynamics displayed by alignment subcomplex might help the PilY1-minor-pilin priming complex enter the T4P machine and to be assembled to the secretin. Once the secretin is stabilized by the minor pilin and PilY1 on either side of its gate, interaction between the alignment subcomplex components PilMNOP and the secretin is strengthened in a coordinated fashion[56] (Fig. 5c).

In the absence of the PilY1-minor-pilin priming complex, minor pseudopilins of the T2SS can prime the production of T4P filaments in *P. aeruginosa*, albeit at a much lower level[15]. However, these pili cannot be recovered from the bacterial cell surface unless the retraction ATPase PilT is deleted. This result suggested that pili primed by the T2SS minor pseudopilins are rapidly retracted by PilT, again pointing to the proposed role of PilY1 in optimizing T4P assembly and dynamics. Since the secretin-priming complex interaction appears to be conditionally essential for T4P biogenesis, our data suggest a potential gate-keeping mechanism regulating the extension and retraction of the pilus filament. As the type IV pilus extends through the polymerization of the major pilin PilA, the minor-pilin complex and PilY1 localized to the pilus tip would move toward the outer membrane and push open the secretin gate. We speculate that after the large PilY1 (~7.5 × 9.5 nm) passes through the PilQ channel, the secretin gate momentarily closes around the thin (~4 nm) apex of the minor pilin complex before it is pushed open again by the extending pilus with a wider dimension of ~5.5 nm (Fig. 5d,e). By contrast, during retraction, the type IV pilus moves in the opposite direction through the T4P machine channel, toward the inner membrane. The dimension of the secretin gate opening would remain constant until the main filament of the pilus formed by major pilins has completely retreated into the secretin, where the gate may then collapse slightly downward to accommodate the thinner dimension (diameter: ~4.2 nm, height: ~18 nm, Supplementary Fig. 10b, c, f, g) of the minor-pilin complex. Thus, when the bulky PilY1 arrives at the secretin, it would not be able to pass through the narrowing gate but instead press against the gate exterior to eventually block secretin entry, stopping pilus retraction at a point where the T4P machine is primed to undergo another cycle of pilus polymerization simply by adding new major pilin subunits at the inner membrane. These data are consistent with previous reports that PilY1 can be both pilus- and cell surface-associated[57]. A recent study suggested that PilY1 in the T4P machine of *M. xanthus* is associated with the minor pilins within the alignment subcomplex below the secretin gate[18,58], thus it remains to be determined whether the PilY1's localization is species dependent. Intriguingly, the *M. xanthus Δ1Δ2Δ3pilY1* T4P structure also showed diminished density for the minor pilins and the alignment subcomplex, consistent with a proposed role of PilY1 in optimizing assembly of the T4P nanomachine. It would be of great interest to determine PilY1-minor pilin subcomplex structure and localization in the different types of T4P machines of diverse bacteria. One limitation of this study is that the subtomogram-averaged structures at 2–4 nm are not sufficient to resolve detailed protein-protein interactions such as those required for the assembly of the minor pilin subcomplex. AlphaFold3 failed to predict a reliable model for the minor pilin subcomplex or its interaction interfaces, key for the formation of the priming complex. These remain important questions in the field remain to be addressed in the future.

Methods

Preparation of cryo-EM grids

For the biofilm sample, *P. aeruginosa* was initially grown overnight in LB with shaking at 37 °C. Next, the culture was diluted to an OD_{600nm} of 0.01 and 5 μL of this diluted culture was deposited onto a freshly glow-discharged gold QUANTIFOIL holey carbon grids (Electron Microscopy Sciences, R2/1 on 200 gold mesh). After ~5 min, the grid was then transferred onto a filter paper on top of the LB agar in a Petri dish. Colony biofilms formed on the grid over the next 16–20 h. PBS with 8–10% glycerol was added and incubated for ~1 min on the grid with the *P. aeruginosa* colony biofilm and then the grid was back blotted for ~5 s before being plunge frozen in liquid ethane, using a homemade, manual plunger-freezing apparatus as described previously[59,60]. A different protocol was used to produce the *P. aeruginosa* cellular samples for determining the subtomogram-averaged structures of the T4P machines. A single colony of *P. aeruginosa* were resuspended in 50 μL of PBS. Next, 5 μL of the resuspended cells were then spotted onto an LB agar plate and incubated at 37 °C for ~12 h. The edges of the resulting colonies were collected and resuspended in PBS to an OD_{600nm} of ~1. After the addition of 10-nm gold fuducial particles the bacterial solution was deposited onto a freshly glow-discharged copper QUANTIFOIL holey carbon grid (Electron Microscopy Sciences, R2/1 on 200 copper mesh). The plunge-freezing procedures followed the protocol described above (no addition of glycerol).

Cryo-FIB milling

The plunge-frozen grids with *P. aeruginosa* biofilms were clipped into cryo-FIB AutoGrids and mounted into the specimen shuttle under liquid nitrogen. An Aquilos2 cryo-FIB system (Thermo Fisher Scientific) was used to mill the thick biofilms into lamellae of <200 nm in thickness. The milling process was previously described[61].

Cryo-ET data acquisition and tomogram reconstruction

Grids containing the resuspended *P. aeruginosa* cells or lamellae of biofilms from cryo-FIB milling were loaded into a 300-kV Titan Krios electron microscope (Thermo Fisher Scientific) equipped with a Direct Electron Detector and energy filter (Gatan) at Yale CryoEM Resource. The FastTOMO script was used with the SerialEM software to collect tilt series with defocus values of approximately −4.8 μm[55], and a cumulative dose of ~70 e^{-}/Å covering angles from −48° to 48° (3° tilt step). Images were acquired at 42,000× magnification with an effective pixel size of 2.148 Å. All recorded images were first drift corrected by MotionCor2[62], stacked by the software package IMOD[63], and then aligned by IMOD using either 10-nm gold particles or Pt particles as fiducial markers. TOMO3D was used to generate tomograms by simultaneous iterative reconstruction technique (SIRT) and weighted-back projection methods[64].

Subtomogram analysis

T4P machines were manually picked from the 6× binned SIRT tomograms, as described[65]. The subtomograms of T4P machines were first selected from the 6× binned tomograms. Next, the i3 software package[66,67] was used for centering and initial alignment of the particles. Multivariate statistical analysis (MSA) was then used with 3-D classification to remove ~30–50% of junk particles. The remaining particles were further centered with translational alignment in i3. MSA with 3D-classification results suggested that the most probably symmetry was c7 (bin4, Supplementary Fig. 2, Supplementary Fig. 4). In addition, the "fitmap" function in ChimeraX was used to generate relative rotational correlation coefficient (CC) of the rotationally aligned subtomogram-averaged structures of the *Pa*-T4P machines. The resulting relative rotational CC values were plotted as a function of rotational degree in Fig. S4d. Afterwards, the subtomograms were extracted from unbinned tomograms with the refined positions and further binned by 2 or 4 based on the requirement for the focused refinement and classification. The final numbers of the T4P machine particles used for subtomogram averaging is shown in Table 1. Fourier shell correlation (FSC) coefficients were calculated by generating the correlation between two randomly divided halves of the aligned images used to estimate the resolution and to generate the final maps[68] (Fig. S3).

Modeling and visualization

Unless otherwise specified, all models of the *Pa*-T4P machine components were generated using AlphaFold/ColabFold (v1.5.3) with the default settings except that the template mode was changed from "none" to "pdb100" (num_relax: 0, template_mode = pdb100, msa_method = mmseqs2, pair_mode = unpaired_paired, model_type = auto, number of cycles = 3, recycle_early_stop_tolerance = auto, pairing_strategy = greedy, max_msa = auto, num_seeds = 1)[31,69]. All *Pa*-T4P machine components have been partially solved to high resolution by X-ray crystallography or cryo-EM, and the use of template structures improve the accuracy of model prediction. For prediction of multi-component complexes, the Alphafold_multimer_v3 embedded in the ColabFold was used where amino-acid sequences of each T4P component were entered in tandem separated by a colon (:). The resulting 5 models predicted by AlphaFold were inspected in ChimeraX and in all cases the top-ranked models were taken for further docking into the segmented cryo-ET densities. The predicted local distance differences test which represents local accuracy (pLDDT), predicted TM-score which corresponds to overall topology accuracy (pTM) and the interface pTM score (ipTM) are summarized in Supplementary Fig. 6, where the snapshots of the models are colored by pLDDT scores. A typical workflow for AlphaFold-assisted molecular modeling is shown in the following example. Structure of the PilQ-TsaP monomeric complex was predicted using AlphaFold multimer V3. The oligomerization states of the PilQ-TsaP complex follow a stoichiometry of 14:7, which is based on the cryo-EM structures of $PilQ_{AMIN1,2\text{-}N0}$ (PDB: 6VE3) and $PilQ_{AMIN1,2\text{-}N0}$ -$TsaP_{CI,II}$ complexes (PDB: 6VE2). The structure was further modified in ChimeraX[70] and Coot[71] to allow the passage of the pilus through the secretin by opening up the PilQ gate (Fig. 1f, g). Some of the low-confidence regions in the resulting AlphaFold models such as the flexible linker regions between $\mathrm{Tsap_{LysM}}$ and $\mathrm{TsaP_{CI\text{-}II}}$ as well as those between $\mathrm{PilQ_{Amin1}}$ and $\mathrm{PilQ_{Amin2}}$ were truncated. The final models of T4P machine components were placed into segmented focus-refined cryo-ET maps and fitted using UCSF ChimeraX "fit to map" function[70]. The correlation coefficient between the models and cryo-ET maps were calculated with PHENIX "Dock in Map"[72]. UCSF ChimeraX[70] was used for surface rendering of subtomogram-averaged structures, segmentation, and molecular modeling. The double-membrane of the Gram-negative bacterium was segmented using EMAN2[73]. The T4P filaments were segmented with the software IMOD. The subtomogram- averaged structures of the piliated and non-piliated T4P machines from the *ΔpilT* and *ΔpilB* cells, the double-membrane and the T4P filaments were mapped back into a wild-type cell using the positions and orientations of the T4P machines in the tomogram with Artiax plug-in in ChimeraX.

Reporting summary

Further information on research design is available in the Nature Portfolio Reporting Summary linked to this article.

Data availability

The focused-refined structures near the outer-membrane region (upper and mid cage-like structures) of the T4P machines from the non-piliated (*ΔpilB*), piliated (*ΔpilT*), *ΔtsaP* and *ΔpilY1* cells generated in this study have been deposited into the Electron Microscopy Data Bank (EMDB) with the accession codes of EMD-43410, EMD-43426, EMD-43433, and EMD-43432, respectively. The focused-refined structures near the inner-membrane region (lower and cytoplasmic cage-like structures) of the T4P machines from the *ΔpilB* and *ΔpilT* cells were deposited into the EMDB with accession codes of EMD-43434 and EMD-43418, respectively.

References

1. Craig, L., Pique, M. E. & Tainer, J. A. Type IV pilus structure and bacterial pathogenicity. *Nat. Rev. Microbiol.* **2**, 363–378 (2004).
2. Burrows, L. L. *Pseudomonas aeruginosa* twitching motility: type IV pili in action. *Annu. Rev. Microbiol.* **66**, 493–520 (2012).
3. Ellison, C. K., Whitfield, G. B. & Brun, Y. V. Type IV pili: dynamic bacterial nanomachines. *FEMS Microbiol. Rev.* **46**, https://doi.org/10.1093/femsre/fuab053 (2022).
4. Siryaporn, A., Kuchma, S. L., O'Toole, G. A. & Gitai, Z. Surface attachment induces *Pseudomonas aeruginosa* virulence. *Proc. Natl. Acad. Sci. USA* **111**, 16860–16865 (2014).
5. Chang, Y. W. et al. Architecture of the *Vibrio cholerae* toxin-coregulated pilus machine revealed by electron cryotomography. *Nat. Microbiol.* **2**, 16269 (2017).
6. Denise, R., Abby, S. S. & Rocha, E. P. C. Diversification of the type IV filament superfamily into machines for adhesion, protein secretion, DNA uptake, and motility. *PLoS Biol.* **17**, e3000390 (2019).
7. Craig, L., Forest, K. T. & Maier, B. Type IV pili: dynamics, biophysics and functional consequences. *Nat. Rev. Microbiol.* **17**, 429–440 (2019).
8. Ellison, C. K. et al. Obstruction of pilus retraction stimulates bacterial surface sensing. *Science* **358**, 535–538 (2017).
9. Whitfield, G. B. & Brun, Y. V. The type IVc pilus: just a Tad different. *Curr. Opin. Microbiol.* **79**, 102468 (2024).
10. Berry, J. L. & Pelicic, V. Exceptionally widespread nanomachines composed of type IV pilins: the prokaryotic Swiss Army knives. *FEMS Microbiol. Rev.* **39**, 134–154 (2015).
11. Chang, Y. W. et al. Architecture of the type IVa pilus machine. *Science* **351**, aad2001 (2016).
12. Gold, V. A., Salzer, R., Averhoff, B. & Kuhlbrandt, W. Structure of a type IV pilus machinery in the open and closed state. *Elife* **4**, https://doi.org/10.7554/eLife.07380 (2015).
13. Jonsson, A. B., Nyberg, G. & Normark, S. Phase variation of gonococcal pili by frameshift mutation in pilC, a novel gene for pilus assembly. *EMBO J.* **10**, 477–488 (1991).
14. Nassif, X. et al. Roles of pilin and PilC in adhesion of *Neisseria meningitidis* to human epithelial and endothelial cells. *Proc. Natl. Acad. Sci. USA* **91**, 3769–3773 (1994).
15. Nguyen, Y. et al. *Pseudomonas aeruginosa* minor pilins prime type IVa pilus assembly and promote surface display of the PilY1 adhesin. *J. Biol. Chem.* **290**, 601–611 (2015).
16. Jacobsen, T., Bardiaux, B., Francetic, O., Izadi-Pruneyre, N. & Nilges, M. Structure and function of minor pilins of type IV pili. *Med Microbiol Immunol.* **209**, 301–308 (2020).
17. Marko, V. A., Kilmury, S. L. N., MacNeil, L. T. & Burrows, L. L. *Pseudomonas aeruginosa* type IV minor pilins and PilY1 regulate virulence by modulating FimS-AlgR activity. *PLoS Pathog.* **14**, e1007074 (2018).
18. Treuner-Lange, A. et al. PilY1 and minor pilins form a complex priming the type IVa pilus in *Myxococcus xanthus*. *Nat. Commun.* **11**, 5054 (2020).
19. Barnier, J. P. et al. The minor pilin PilV provides a conserved adhesion site throughout the antigenically variable meningococcal type IV pilus. *Proc. Natl. Acad. Sci. USA* **118**, https://doi.org/10.1073/pnas.2109364118 (2021).
20. Winther-Larsen, H. C. et al. A conserved set of pilin-like molecules controls type IV pilus dynamics and organelle-associated functions in *Neisseria gonorrhoeae*. *Mol. Microbiol.* **56**, 903–917 (2005).
21. Orans, J. et al. Crystal structure analysis reveals *Pseudomonas* PilY1 as an essential calcium-dependent regulator of bacterial surface motility. *Proc. Natl. Acad. Sci. USA* **107**, 1065–1070 (2010).
22. Hoppe, J. et al. PilY1 promotes *Legionella pneumophila* infection of human lung tissue explants and contributes to bacterial adhesion, host cell invasion, and twitching motility. *Front Cell Infect. Microbiol.* **7**, 63 (2017).
23. Kuchma, S. L. et al. Cyclic-di-GMP-mediated repression of swarming motility by *Pseudomonas aeruginosa*: the pilY1 gene and its impact on surface-associated behaviors. *J. Bacteriol.* **192**, 2950–2964 (2010).
24. Luo, Y. et al. A hierarchical cascade of second messengers regulates *Pseudomonas aeruginosa* surface behaviors. *Mbio* **6**, https://doi.org/10.1128/mBio.02456-14 (2015).
25. Koo, J., Lamers, R. P., Rubinstein, J. L., Burrows, L. L. & Howell, P. L. Structure of the *Pseudomonas aeruginosa* type IVa pilus secretin at 7.4 A. *Structure* **24**, 1778–1787 (2016).
26. Weaver, S. J. et al. CryoEM structure of the type IVa pilus secretin required for natural competence in *Vibrio cholerae*. *Nat. Commun.* **11**, 5080 (2020).
27. McCallum, M., Tammam, S., Rubinstein, J. L., Burrows, L. L. & Howell, P. L. CryoEM map of *Pseudomonas aeruginosa* PilQ enables structural characterization of TsaP. *Structure* **29**, 457–466 e454 (2021).
28. Tassinari, M., Rudzite, M., Filloux, A. & Low, H. H. Assembly mechanism of a Tad secretion system secretin-pilotin complex. *Nat. Commun.* **14**, 5643 (2023).
29. Siewering, K. et al. Peptidoglycan-binding protein TsaP functions in surface assembly of type IV pili. *Proc. Natl. Acad. Sci. USA* **111**, E953–E961 (2014).
30. Liu, J. et al. Enhancing alphafold-multimer-based protein complex structure prediction with MULTICOM in CASP15. *Commun. Biol.* **6**, 1140 (2023).
31. Mirdita, M. et al. ColabFold: making protein folding accessible to all. *Nat. Methods* **19**, 679–682 (2022).
32. Tammam, S. et al. PilMNOPQ from the *Pseudomonas aeruginosa* type IV pilus system form a transenvelope protein interaction network that interacts with PilA. *J. Bacteriol.* **195**, 2126–2135 (2013).

33. Tammam, S. et al. Characterization of the PilN, PilO and PilP type IVa pilus subcomplex. *Mol. Microbiol.* **82**, 1496–1514 (2011).
34. Korotkov, K. V. et al. Structural and functional studies on the interaction of GspC and GspD in the type II secretion system. *PLoS Pathog.* **7**, e1002228 (2011).
35. McCallum, M., Burrows, L. L. & Howell, P. L. The dynamic structures of the type IV pilus. *Microbiol. Spectr.* **7**, https://doi.org/10.1128/microbiolspec.PSIB-0006-2018 (2019).
36. Leighton, T. L., Yong, D. H., Howell, P. L. & Burrows, L. L. Type IV pilus alignment subcomplex proteins PilN and PilO form homo- and heterodimers in vivo. *J. Biol. Chem.* **291**, 19923–19938 (2016).
37. Karuppiah, V., Collins, R. F., Thistlethwaite, A., Gao, Y. & Derrick, J. P. Structure and assembly of an inner membrane platform for initiation of type IV pilus biogenesis. *Proc. Natl. Acad. Sci. USA* **110**, E4638–E4647 (2013).
38. Sampaleanu, L. M. et al. Periplasmic domains of *Pseudomonas aeruginosa* PilN and PilO form a stable heterodimeric complex. *J. Mol. Biol.* **394**, 143–159 (2009).
39. McCallum, M. et al. PilN binding modulates the structure and binding partners of the *Pseudomonas aeruginosa* type IVa pilus protein PilM. *J. Biol. Chem.* **291**, 11003–11015 (2016).
40. Karuppiah, V. & Derrick, J. P. Structure of the PilM-PilN inner membrane type IV pilus biogenesis complex from *Thermus thermophilus*. *J. Biol. Chem.* **286**, 24434–24442 (2011).
41. Georgiadou, M., Castagnini, M., Karimova, G., Ladant, D. & Pelicic, V. Large-scale study of the interactions between proteins involved in type IV pilus biology in *Neisseria meningitidis*: characterization of a subcomplex involved in pilus assembly. *Mol. Microbiol.* **84**, 857–873 (2012).
42. Liu, X. et al. Bacterial flagella hijack type IV pili proteins to control motility. *Proc. Natl. Acad. Sci. USA* **121**, e2317452121 (2024).
43. McCallum, M. et al. Multiple conformations facilitate PilT function in the type IV pilus. *Nat. Commun.* **10**, 5198 (2019).
44. McCallum, M., Tammam, S., Khan, A., Burrows, L. L. & Howell, P. L. The molecular mechanism of the type IVa pilus motors. *Nat. Commun.* **8**, 15091 (2017).
45. Ochner, H. et al. Structure of the Pseudomonas aeruginosa PAO1 Type IV pilus. bioRxiv 2024 https://doi.org/10.1101/2024.04.09.588664 (2024).
46. Thongchol, J. et al. Removal of *Pseudomonas* type IV pili by a small RNA virus. *Science* **384**, eadl0635 (2024).
47. Pelicic, V. Mechanism of assembly of type 4 filaments: everything you always wanted to know (but were afraid to ask). *Microbiology* **169**, https://doi.org/10.1099/mic.0.001311 (2023).
48. Guilvout, I. et al. Membrane platform protein PulF of the *Klebsiella* type II secretion system forms a trimeric ion channel essential for endopilus assembly and protein secretion. *Mbio* **15**, e0142323 (2024).
49. Johnson, M. D. et al. *Pseudomonas aeruginosa* PilY1 binds integrin in an RGD- and calcium-dependent manner. *PLoS ONE* **6**, e29629 (2011).
50. Webster, S. S., Wong, G. C. L. & O'Toole, G. A. The power of touch: type 4 pili, the von Willebrand A domain, and surface sensing by *Pseudomonas aeruginosa*. *J. Bacteriol.* **204**, e0008422 (2022).
51. Islam, S. T. et al. Unmasking of the von Willebrand A-domain surface adhesin CglB at bacterial focal adhesions mediates myxobacterial gliding motility. *Sci. Adv.* **9**, eabq0619 (2023).
52. Guo, S., Vance, T. D. R., Stevens, C. A., Voets, I. & Davies, P. L. RTX adhesins are key bacterial surface megaproteins in the formation of biofilms. *Trends Microbiol* **27**, 453–467 (2019).
53. Beaussart, A. et al. Nanoscale adhesion forces of *Pseudomonas aeruginosa* type IV Pili. *ACS Nano* **8**, 10723–10733 (2014).
54. Anyan, M. E. et al. Type IV pili interactions promote intercellular association and moderate swarming of *Pseudomonas aeruginosa*. *Proc. Natl Acad. Sci. USA* **111**, 18013–18018 (2014).
55. Xu, A. & Xu, C. FastTomo: a SerialEM script for collecting electron tomography data. *bioRxiv*, 2021.2003.2016.435675 https://doi.org/10.1101/2021.03.16.435675 (2021).
56. Carter, T. et al. The type IVa pilus machinery is recruited to sites of future cell division. *Mbio* **8**, https://doi.org/10.1128/mBio.02103-16 (2017).
57. Bohn, Y. S. et al. Multiple roles of *Pseudomonas aeruginosa* TBCF10839 PilY1 in motility, transport and infection. *Mol. Microbiol.* **71**, 730–747 (2009).
58. Herfurth, M., Perez-Burgos, M. & Sogaard-Andersen, L. The mechanism for polar localization of the type IVa pilus machine in *Myxococcus xanthus*. *Mbio* **14**, e0159323 (2023).
59. Liu, J. et al. Intact flagellar motor of *Borrelia burgdorferi* revealed by cryo-electron tomography: evidence for stator ring curvature and rotor/C-ring assembly flexion. *J. Bacteriol.* **191**, 5026–5036 (2009).
60. Zhao, X. et al. Cryoelectron tomography reveals the sequential assembly of bacterial flagella in *Borrelia burgdorferi*. *Proc. Natl. Acad. Sci. USA* **110**, 14390–14395 (2013).
61. Xiang, Y. et al. Interconnecting solvent quality, transcription, and chromosome folding in *Escherichia coli*. *Cell* **184**, 3626–3642 e3614 (2021).
62. Zheng, S. Q. et al. MotionCor2: anisotropic correction of beam-induced motion for improved cryo-electron microscopy. *Nat. Methods* **14**, 331–332 (2017).
63. Kremer, J. R., Mastronarde, D. N. & McIntosh, J. R. Computer visualization of three-dimensional image data using IMOD. *J. Struct. Biol.* **116**, 71–76 (1996).
64. Agulleiro, J. I. & Fernandez, J. J. Tomo3D 2.0-exploitation of advanced vector extensions (AVX) for 3D reconstruction. *J. Struct. Biol.* **189**, 147–152 (2015).
65. Zhu, S., Qin, Z., Wang, J., Morado, D. R. & Liu, J. In-situ structural analysis of the spirochetal flagellar motor by cryo-electron tomography. *Methods Mol. Biol.* **1593**, 229–242 (2017).
66. Winkler, H. 3D reconstruction and processing of volumetric data in cryo-electron tomography. *J. Struct. Biol.* **157**, 126–137 (2007).
67. Winkler, H. et al. Tomographic subvolume alignment and subvolume classification applied to myosin V and SIV envelope spikes. *J. Struct. Biol.* **165**, 64–77 (2009).
68. Guo, S., Xu, H., Chang, Y., Motaleb, M. A. & Liu, J. FliL ring enhances the function of periplasmic flagella. *Proc. Natl. Acad. Sci. USA* **119**, e2117245119 (2022).
69. Jumper, J. et al. Highly accurate protein structure prediction with AlphaFold. *Nature*, https://doi.org/10.1038/s41586-021-03819-2 (2021).
70. Goddard, T. D. et al. UCSF ChimeraX: meeting modern challenges in visualization and analysis. *Protein Sci.* **27**, 14–25 (2018).
71. Emsley, P. & Cowtan, K. Coot: model-building tools for molecular graphics. *Acta Crystallogr. D. Biol. Crystallogr.* **60**, 2126–2132 (2004).
72. Afonine, P. V. et al. New tools for the analysis and validation of cryo-EM maps and atomic models. *Acta Crystallogr. D. Struct. Biol.* **74**, 814–840 (2018).
73. Tang, G. et al. EMAN2: an extensible image processing suite for electron microscopy. *J. Struct. Biol.* **157**, 38–46 (2007).

Acknowledgements

We thank Shiwei Zhu for performing initial cryo-ET experiments for this work. We are grateful to Ms. Jennifer Aronson for her critical reading and editing of the manuscript. This work was supported in part by grant PJT-169053 from the Canadian Institutes of Health Research (CIHR) to L.L.B, P.L.H, Y.V.B and J.L.; S.G., Y.C., and J.L. were partly supported by NIH grants R01AI087946, R01AI152421 and R01AI132818; S.G. was also supported by a CIHR Fellowship and a start-up fund by the Faculty of Medicine and Health Sciences at McGill University. L.L.B. holds a Tier I Canada Research Chair in Microbe-Surface Interactions (CRC 2021-

00103). Y.V.B. was supported by a Canada 150 Research Chair from the CIHR. P.L.H. was the recipient of a Tier I Canada Research Chair in Structural Biology from 2006-2020. We thank Shenping Wu at the Yale Cryo-EM resources for assistance with cryo-ET data collection, which was funded in part by the NIH grant 1S10OD023603-01A1.

Author contributions

S.G., L.L.B., Y.V.B., P.L.H., and J.L. conceived the project. S.G. performed cryo-ET, cryo-FIB experiments, and data analyses with Y.C. S.G. performed integrative modeling and prepared the initial manuscript with input from L.L.B. and J.L. S.G. revised the manuscript with editorial input from all authors.

Competing interests

The authors declare no competing interests.

Additional information

Supplementary information The online version contains supplementary material available at https://doi.org/10.1038/s41467-024-53638-y.

Correspondence and requests for materials should be addressed to Shuaiqi Guo, Lori L. Burrows or Jun Liu.

Peer review information *Nature Communications* thanks Anastasia D. Gazi and the other, anonymous, reviewer(s) for their contribution to the peer review of this work. A peer review file is available.

Reprints and permissions information is available at http://www.nature.com/reprints

Publisher's note Springer Nature remains neutral with regard to jurisdictional claims in published maps and institutional affiliations.

Open Access This article is licensed under a Creative Commons Attribution-NonCommercial-NoDerivatives 4.0 International License, which permits any non-commercial use, sharing, distribution and reproduction in any medium or format, as long as you give appropriate credit to the original author(s) and the source, provide a link to the Creative Commons licence, and indicate if you modified the licensed material. You do not have permission under this licence to share adapted material derived from this article or parts of it. The images or other third party material in this article are included in the article's Creative Commons licence, unless indicated otherwise in a credit line to the material. If material is not included in the article's Creative Commons licence and your intended use is not permitted by statutory regulation or exceeds the permitted use, you will need to obtain permission directly from the copyright holder. To view a copy of this licence, visit http://creativecommons.org/licenses/by-nc-nd/4.0/.

© The Author(s) 2024